JPE 13-4-7

http://dx.doi.org/10.6113/JPE.2013.13.4.558

Analysis and Design of a Three-port Flyback Inverter using an Active Power Decoupling Method to Minimize Input Capacitance

Jun-Gu Kim*, Kyu-Dong Kim**, Yong-Su Noh*, Yong-Chae Jung***, and Chung-Yuen Won†

*†College of Information and Communication Eng., Sungkyunkwan University, Suwon, Korea
**Samsung Electro-Mechanics Co. Ltd., Suwon, Korea
***Dept. of Electrical and Electronics Eng., Namseoul University, Cheonan, Korea

Abstract

In this paper, a new decoupling technique for a flyback inverter using an active power decoupling circuit with auxiliary winding and a novel switching pattern is proposed. The conventional passive power decoupling method is applied to control Maximum Power Point Tracking (MPPT) efficiently by attenuating double frequency power pulsation on the photovoltaic (PV) side. In this case, decoupling capacitor for a flyback inverter is essentially required large electrolytic capacitor of milli-farads. However using the electrolytic capacitor have problems of bulky size and short life-span. Because this electrolytic capacitor is strongly concerned with the life-span of an AC module system, an active power decoupling circuit to minimize input capacitance is needed. In the proposed topology, auxiliary winding defined as a Ripple port will partially cover difference between a PV power and an AC Power. Since input capacitor and auxiliary capacitor is reduced by Ripple port, it can be replaced by a film capacitor. To perform the operation of charging/discharging decoupling capacitor C_x, a novel switching sequence is also proposed. The proposed topology is verified by design analysis, simulation and experimental results.

Key words: Active power decoupling, Three-port flyback inverter, Film capacitor.

I. INTRODUCTION

The AC module system has received great attention for photovoltaic power conversion devices. This system which is attached behind each photovoltaic (PV) panel fulfills the DC to AC conversion. Also it is called a micro inverter which contrasts with other kinds of grid interactive photovoltaic inverter including conventional string and central type inverters. The AC module PV inverter has several advantages compared with conventional systems. First, it can plug and play with each PV panel, thus maintenance and substitution is easy. Second, each micro inverter is performing maximum power point tracking (MPPT) for each panel, so it is strong enough to produce PV energy, even in difficult conditions, such as shading, fallen leaves or snow in such a solar panel [1]-[5].

Generally, the AC module system is adjusted to a single-phase grid-connected inverter generating small power under 500[W]. When the DC power from the PV panel is converted to the AC utility, large voltage pulsation occurs in the DC-link. These single-phase DC and AC coupling systems need a large capacitance at DC-link, to suppress voltage ripple doubled with grid frequency [6]. This is called a power decoupling technique, and requires energy storage components like an inductor or capacitor in which the energy variation will charge and discharge. A multi-stage inverter including a two-stage structure connected DC-DC converter and DC-AC inverter does not require such a power decoupling technique because DC-link of two-stage system maintains high voltage which is greater than utility peak voltage [5]. However, the micro inverter using single-stage a flyback type especially needs large input capacitance to manage power fluctuation, because it has pseudo DC-link structure. This input capacitor stores surplus PV energy and supplies deficient energy, so the entire system can obtain good MPPT performance without the

Manuscript received Jan. 29, 2013; revised Apr. 25, 2013
Recommended for publication by Associate Editor Jin Hur.
†Corresponding Author: woncy@skku.edu
Tel: +82-31-290-7115, Fax: +82-31-299-4623, Sungkyunkwan University
*College of Information and Communication Eng., Sungkyunkwan Univ., Korea
**Samsung Electro-Mechanics Co. Ltd.
***Dept. Of Electrical and Electronics Eng., Namseoul University, Cheonan, Korea

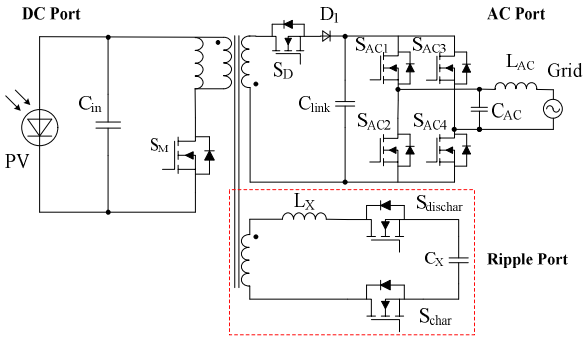

Fig. 1. Configuration of proposed topology.

voltage pulsation.

However, these systems using a large electrolytic capacitor for the power decoupling have some serious drawbacks [5]. First of all, a large volume of capacitor makes the system size bulky, because input capacitance of the conventional flyback inverter has milli-farads. Second, the electrolytic capacitor commonly has a short life-span of about 5000 hours in general operating conditions. Because the life-span of a micro inverter is strongly concerned with lifetime of electrolytic capacitor, an active power decoupling technique should be applied to overcome reliability problem.

In the flyback type micro inverter, many active power decoupling techniques using a subsidiary circuit in the PV side are studied. Decoupling techniques of PV side have to use an auxiliary circuit and a decoupling capacitor of this circuit will carry out charge and discharge of the surplus and shortage energy. This technique can reduce capacitance of input capacitor, thus the electrolytic capacitor which is located on the input side can be replaced by a film capacitor. Early studies of PV side decoupling used a subsidiary decoupling circuit which is connected in parallel with input side of system. A parallel decoupling configuration makes for low system efficiency because of many switches and passive components [7]-[16].

Recently, some researches for a three-port type flyback inverter have been carried out [17]-[20]. These types have less components in the decoupling circuit by using auxiliary winding. In the paper, a new type of three-port flyback inverter using an additional decoupling port which covers surplus and shortage energy and behaves as a charging or discharging decoupling capacitor is proposed. Furthermore the proposed flyback inverter is designed for application to a 250[W] PV module integrated converter (MIC) The decoupling sequence will be defined by the switching pattern and this will be proved by mode analysis. From this design process, the duty of each switch and block diagram is determined for implementing the simulation and experiment of this proposed topology.

II. PROPOSED TOPOLOGY

A. Conventional Flyback Inverter for Applying PV-MIC

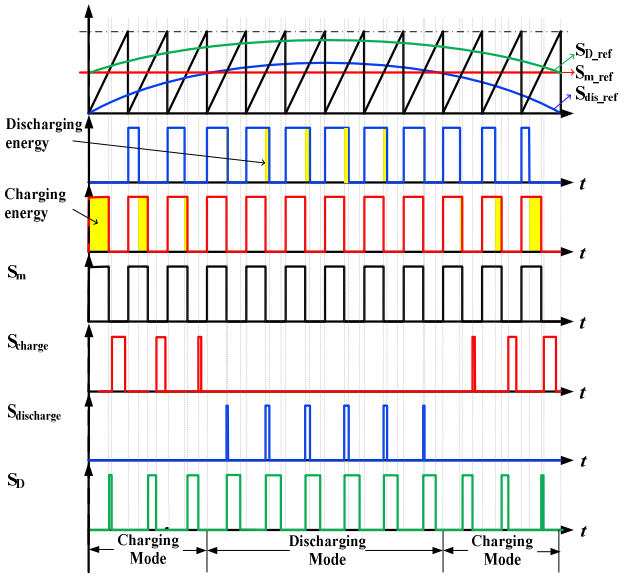

Fig. 2. Switching patterns of proposed topology.

Fig. 1 shows the configuration of proposed topology. The proposed a three-port type flyback inverter is configured by DC port, AC port and Ripple port. First, the DC port is directly connected to the PV panel and consists of flyback transformer and main switch S_M. The AC port is composed of synchronous switch S_D, DC-link and unfolding bridge inverter which is connected with the grid. This type of inverter is operated as an unfolder synchronized with the grid, and an unfolding bridge. Lastly the Ripple port to deal with surplus and shortage energy is made by auxiliary winding. Also Ripple port is configured as a small value of the inductor to attenuate switching frequency and prevent drastic current flow to the capacitor, auxiliary switch S_{charge}, $S_{discharge}$ and decoupling capacitor C_x. Generally, these subsidiary circuits are needed more than two switches to make bidirectional power flow. In this topology, only two switches are used for charging and discharging the decoupling capacitor in the Ripple port, which is a simplified structure compared with the conventional three-port decoupling circuit [20].

B. Definition of Switching Sequence

Fig. 2 shows the switching sequence. Fig. 3 shows two dominant modes, one is called the charging mode which the decoupling capacitor C_x of Ripple port and the other is the discharging mode. Typically the mode of charging/discharging is defined by comparing the DC input power P_{in} and instantaneous output power p_{out}. When the input power is larger than the output power (i.e. $P_{in} > p_{out}$), surplus energy has to be charged in the decoupling capacitor. Also, when the input power is smaller than the output power (i.e. $P_{in} < p_{out}$), then the shortage power is supplied by the already charged energy in decoupling capacitor.

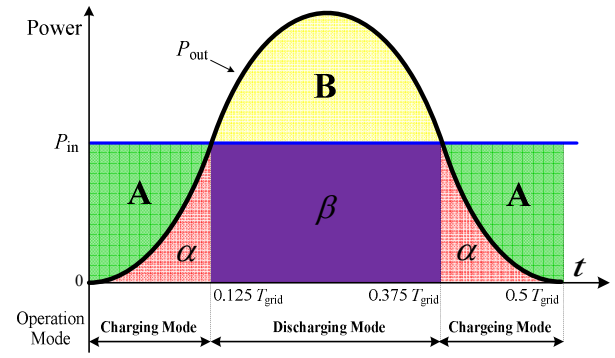

(a) The input and output power.

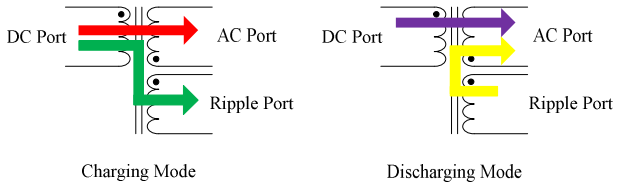

(b) Power flow of charge and discharge mode.

Fig. 3. Power of AC module and Power flow of each operating mode.

This flyback inverter is operated in discontinuous conduction mode (DCM) condition because of satisfying the current source behavior [21]. To make a rectified sine wave, this voltage-controlled current-source operation is necessary. And a secondary side inverter should be operate as an unfolder to grid interconnection. The main switch S_M is turned on fixed duty. This duty is defined by the MPPT control to transfer maximum power to grid. The actual value of the magnetizing current will be compared to the reference current which is calculated as the maximum value of i_{Lm}.

III. Mode Analysis

Mode 1-1 : The main switch S_M is turned on fixed duty and other switches are turned off. d_1 is the main switch turn-on duration. During Mode 1-1, the magnetizing inductor L_m is storing energy and the magnetizing current i_{Lm} increases linearly until reaching the peak current $i_{Lm(peak)}$. This peak current calculated in (2) is derived by MPPT control which makes a constant value of input current from the PV panel. The duration of the main switch being turned on is calculated in (3).

$$i_{Lm}(t) = \frac{V_{in}}{L_m}(t - T_0) \tag{1}$$

$$i_{Lm(peak)} = i_{Lm}(T_1) = \frac{V_{in}}{L_m}(T_1 - T_0) = \frac{V_{in}}{L_m} d_1 T_s \tag{2}$$

$$d_1 T_s = \frac{L_m}{V_{in}} i_{Lm(peak)} \tag{3}$$

Mode 1-2A : In this mode, the AC side switch S_D is turned on and the energy stored in the magnetizing inductor is delivered to the AC port. This magnetizing energy is discharged at the end(T_{2A}) of Mode 1-2A. Mode 1-2A and the next Mode 1-3A are activated near the time when the instantaneous power p_{out} is lower than the input power P_{in}.

$$i_s(t) = \frac{N_p}{N_s} i_{Lm(peak)} - \left(\frac{N_p}{N_s}\right)^2 \frac{v_{AC}}{L_m}(t - T_1) \tag{4}$$

$$d_{2A} T_s = \left(\frac{N_s}{N_p}\right)^2 \frac{L_m}{V_{AC}} \left(\frac{N_p}{N_s} i_{Lm(peak)} - i_{s(peak)}\right) \tag{5}$$

Mode 1-3A : In this mode, surplus energy is managed by the subsidiary port for power decoupling and the auxiliary switch S_{charge} is turned on. The decoupling capacitor C_x is charged from the remaining magnetizing energy. The Ripple port current i_x is derived in (6), if the V_x is applied constantly in the decoupling capacitor C_x.

$$i_x(t) = \frac{N_p}{N_x} i_{s(peak)} - \left(\frac{N_p}{N_x}\right)^2 \frac{V_x}{L_m + \left(\frac{N_p}{N_x}\right)^2 L_2}(t - T_{2A}) \tag{6}$$

$$d_{3A} T_s = \left(\frac{N_x}{N_p}\right) \frac{L_m + \left(\frac{N_p}{N_x}\right)^2 L_2}{V_x} i_{s(peak)} \tag{7}$$

Mode 1-4A : There is no power flow from the DC to AC port because of DCM operation. All switches are turned off.

Mode 1-2B and Mode 1-3B : There is no power flow to the Ripple port. In this duration in which the main switch is turned off, the energy stored in the magnetizing inductor is transferred to the AC port only.

$$i_s(t) = \frac{N_p}{N_s} i_{Lm(peak)} - \left(\frac{N_p}{N_s}\right)^2 \frac{v_{AC}}{L_m}(t - T_1) \tag{8}$$

$$d_{2B} T_s = \left(\frac{N_s}{N_p}\right) \frac{L_m}{v_{AC}} i_{Lm(peak)} \tag{9}$$

Mode 2-1 : The operation of this mode is the same as Mode 1-1, charging the decoupling capacitor mode.

Mode 2-2A : In this mode, the synchronous switch S_D which is located on the front side of the AC port is turned on and the discharging switch $S_{discharge}$ on the decoupling port is also activated at the same time. The discharged energy from the decoupling capacitor is delivered to the AC port when the PV energy is insufficient ($P_{in} < p_{out}$).

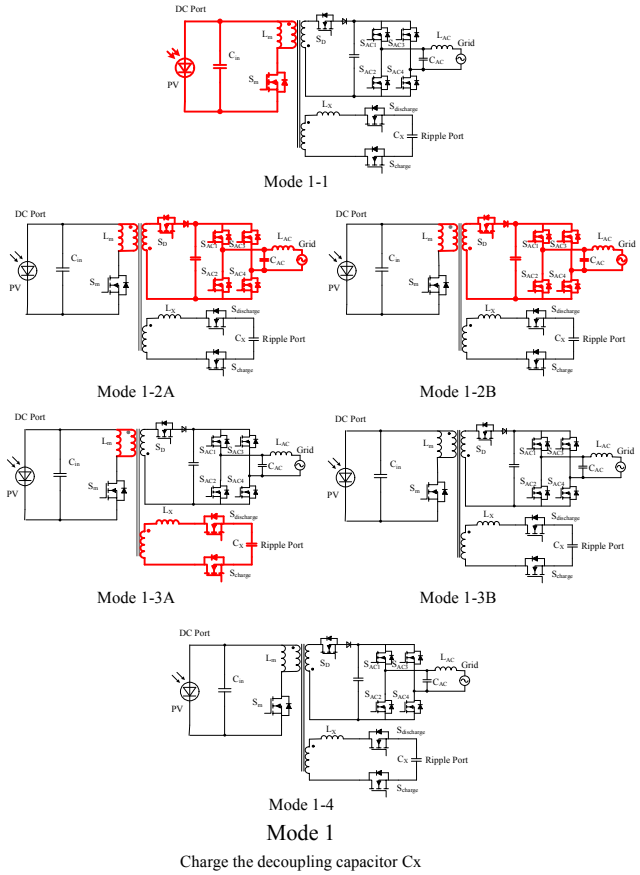

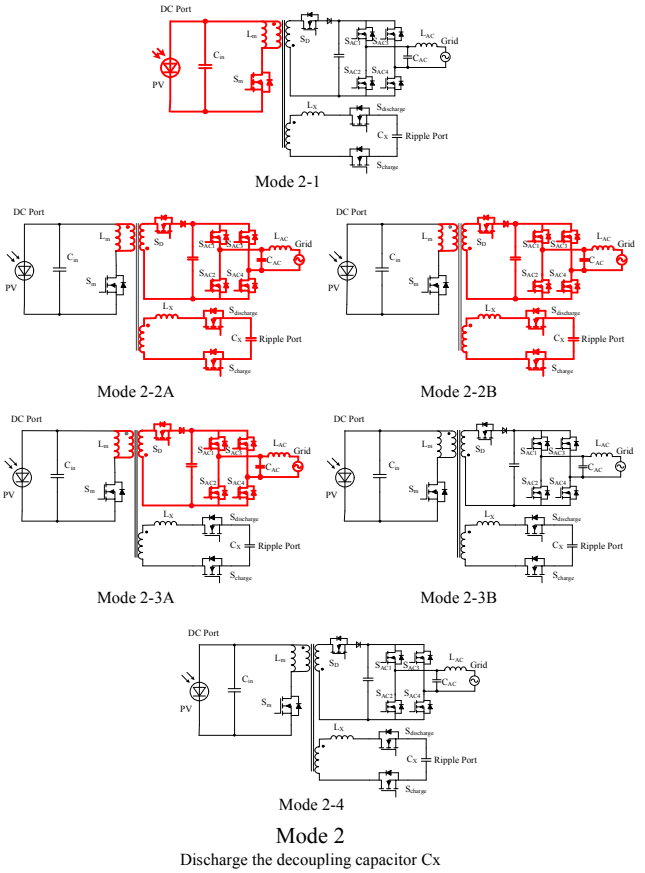

Fig. 4. The operation modes of each stage.

$$i_{s1}(t)=\left(\frac{N_p}{N_s}\right)i_{Lm(peak)}-\left\{\left(\frac{N_p}{N_s}\right)^2\frac{v_{AC}}{L_m}-\left(\frac{N_x}{N_s}\right)^2\frac{V_x}{L_x}\right\}(t-T_1) \tag{10}$$

$$d_{2A}T_s=\frac{\left(\frac{N_p}{N_s}\right)i_{Lm(peak)}-i_{s1(peak)}}{\left(\frac{N_p}{N_s}\right)^2\frac{v_{AC}}{L_m}-\left(\frac{N_x}{N_s}\right)^2\frac{V_x}{L_x}} \tag{11}$$

Mode 2-3A : The operation of discharging the decoupling capacitor has just finished at the end of Mode 2-2A and then the remaining magnetizing energy is delivered to the secondary port. In this mode, S_{charge} and $S_{discharge}$ maintain the turn-off state and the synchronous switch S_D on the AC port is turned on.

$$i_{s2}(t)=i_{s1(peak)}-\left(\frac{N_p}{N_s}\right)^2\frac{v_{AC}}{L_m}(t-T_{2A}) \tag{12}$$

$$d_{3A}T_s=\left(\frac{N_s}{N_p}\right)^2\frac{L_m}{v_{AC}}i_{s1(peak)} \tag{13}$$

Mode 2-2B : This mode has the same operation as Mode 2-2A.

Mode 2-3B : The stored energy in the magnetizing inductor is fully discharged in the former Mode 2-2B. The switch $S_{discharge}$ for discharging the decoupling capacitor still maintains a turn-on state so remaining energy in this capacitor is transferred to the primary side. This makes a negative current path on the primary side and the magnetizing inductor is charged again.

$$i_x(t)=\left(\frac{N_p}{N_x}\right)^2\frac{V_x}{L_m+\left(\frac{N_p}{N_x}\right)^2L_x}(t-T_{2B})-\frac{N_p}{N_x}i_{s(peak)} \tag{14}$$

$$d_{3B}T_s=\left(\frac{N_x}{N_p}\right)\frac{L_m+\left(\frac{N_p}{N_x}\right)L_x}{V_x}i_{s(peak)} \tag{15}$$

Mode 2-4 : In the discharging mode, the proposed converter is also operated in DCM condition and all switches are turned off.

Finally, the magnetizing inductance L_m satisfying the DCM condition could be calculated by (16) below concerning the total duty cycle :

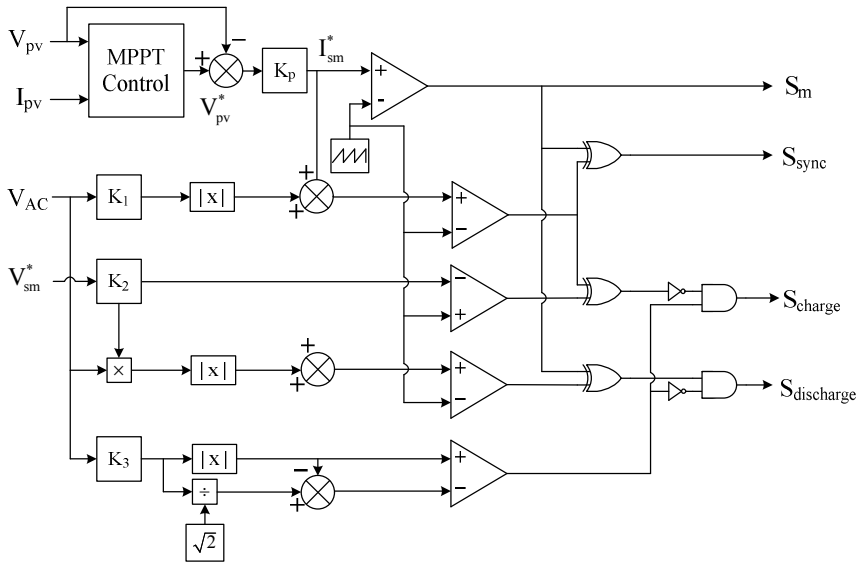

Fig. 5. The control block diagram for processing the proposed decoupling operation.

$$d_1 T_s + d_{2A} T_s + d_{3A} T_s < T_s \tag{16}$$

$$d_1 T_s + d_{2B} T_s < T_s \tag{17}$$

By substituting (3), (5), and (7) into (16), we can obtain

$$\left(\frac{L_m}{V_{in}} + \left(\frac{N_s}{N_p}\right)\frac{L_m}{V_{AC}\sin\omega t}\right) i_{Lm(peak)} + \left(\left(\frac{N_x}{N_p}\right)\frac{L_m + \left(N_p / N_x\right)^2 L_x}{V_x} - \left(\frac{N_s}{N_p}\right)^2 \frac{L_m}{V_{AC}\sin\omega t}\right) i_{s(peak)} < T_s$$

$$\left(\left(\frac{N_x}{N_p}\right)\frac{L_m + \left(N_p / N_x\right)^2 L_x}{V_x} - \left(\frac{N_s}{N_p}\right)^2 \frac{L_m}{V_{AC}\sin\omega t}\right) i_{s(peak)} + \left(\frac{L_m}{V_{in}} + \left(\frac{N_s}{N_p}\right)\frac{L_m}{V_{AC}\sin\omega t}\right) i_{Lm(peak)} < T_s \tag{18}$$

In (18), $i_{Lm(peak)}$ and $i_{s(peak)}$ value are not defined. The peak current of the magnetizing inductor is derived from the averaged input power P_{in}.

$$P_{in} = V_{in} I_{in} = \frac{L_m i_{Lm(peak)}^{\ 2}}{2T_s} \tag{19}$$

$$P_{out} = \frac{1}{2} V_{AC} I_{AC} \tag{20}$$

On the assumption that the power conversion efficiency is neglected (i.e. $P_{in} = P_{out}$). So the current $i_{Lm(peak)}$ is derived by

$$i_{Lm(peak)} = \sqrt{\frac{V_{AC} I_{AC} T_s}{L_m}} \tag{21}$$

And the peak current of the secondary side, $i_{s(peak)}$ is calculated by

$$i_{s(peak)} = \left(\frac{N_p}{N_s}\right) i_{Lm(peak)} \left|\sin\omega t\right| \tag{22}$$

By substituting (3), (7), (18), (19) and (20) into (17), L_m will be derived by (22).

$$L_m < \frac{T_s}{V_{AC} I_{AC}} \left(\frac{V_{AC} \cdot V_{in}}{V_{AC} + \sqrt{2}\left(N_s / N_p\right) V_{in}}\right)^2 \tag{23}$$

From (23) adjusting the design specification for a 250[W] flyback inverter, the maximum magnetizing inductance for satisfying the DCM condition is calculated by 15[μH]. Because this inductance is tight with the boundary condition, L_m is selected by 10[μH] with considering a sufficient margin.

In this proposed three-port type active power decoupling technique, a differentiated control scheme is induced to satisfy the charge/discharge mode for a decoupling capacitor as shown in Fig. 5. This control block including reference value and control logic sequence is designed after determine of the proposed converter circuit parameters. This control block makes four switching signals to control the main switch, secondary synchronous switch and auxiliary charge/discharge switch. A constant value of PV voltage from MPPT control works as a reference value which is compared with the carrier signal. That makes a fixed duty for the main switch S_m. The other switching signals are not linked with the gate of the output signal S_m, because the other switches are activated after the main switch is turned off. These switches including the synchronous switch and auxiliary switches have to be controlled in the manner of comparing the rectified reference sine wave with the carrier wave to make rectified link voltage.

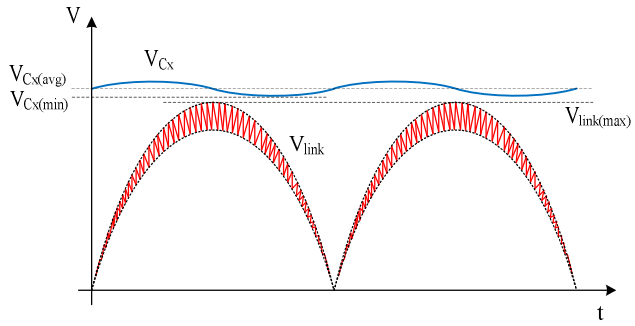

Fig. 6. Comparison for satisfying specific condition between Ripple port voltage V_{Cx} and secondary side rectified voltage V_{link}.

IV. Comparison with the Input Capacitance

The proposed topology is based on a flyback inverter having DCM operation. So, the magnetized inductance satisfying DCM and the maximum feasible duty of each switch has to be set as design restrictions. The magnetizing inductance L_m satisfying DCM condition is as in (23).

The maximum duty of each switch satisfying DCM by selecting the magnetized inductor can be induced with (24) and (25). The calculated maximum duty is 0.74 using Table II. In this paper, fixed duty 0.5 is used in consideration of a margin.

$$L_m \le \frac{(V_{in} d_{sm,DCM})^2}{4 V_{AC} I_{AC} f_s} \tag{24}$$

$$d_{sm,DCM} \le \frac{\sqrt{4 L_m V_{AC} I_{AC} f_s}}{V_{in}} = 0.74 \tag{25}$$

The formula deciding the circuit section of the secondary switch in turn-off of the main switch is as follows. With the calculated value in (27), the turn-on duty of the secondary switch has to be met as 0.24 at least.

$$t_{off} = \frac{(N_p / N_s) V_{in} T_s d_{sm,pk}}{V_{ac,pk}} \tag{26}$$

$$d_{sync} = \frac{(N_p / N_s) V_{in} T_s d_{sm}}{V_{ac,pk}} = 0.24 \tag{27}$$

To prevent distortion of the output current, the voltage of the Ripple port has to be larger than the applied voltage across the DC-link voltage. The power flow is decided depending on the magnitude relationship with each voltage, and if it failed to meet the above condition, energy transfer in the output of the Ripple port would not happen, and creating distortion of the output current. Fig. 6 shows the relation of the rectified sine wave type voltage V_{link} applied to the secondary DC-link with the voltage of the tertiary side capacitor, V_{Cx} which has ripple voltage with double the grid frequency in the Ripple port.

To make power flow to the secondary port, it is required relationship between V_{sec} and V_{Cx}. This condition is induced by the condition connected with the secondary diode.

$$V_{\sec} = V_{Cx} \times \frac{N_s}{N_x} > V_{link} \tag{28}$$

$$V_{Cx(\min)} \times \frac{N_s}{N_x} > V_{link(\max)} \tag{29}$$

The equation (30) shows the average voltage value applied to the capacitor of the Ripple port $V_{Cx(avg)}$, and the average value is decided by the inductor and tertiary turn value based on (31).

$$V_{Cx(avg)} = V_{tri} + V_{Lx} \tag{30}$$

$$\begin{aligned} &V_{Lx} \uparrow \Rightarrow V_{tri} \uparrow \\ &L_x \uparrow \Rightarrow V_{Lx} \uparrow \Rightarrow V_{Cx(avg)} \uparrow \end{aligned} \tag{31}$$

The equation (31) shows that larger average voltage of the decoupling capacitor C_x is better for securing a margin to prevent output current distortion.

With the above design consideration, the tertiary inductor value for preventing output current distortion can be calculated, and bigger inductance allows a larger margin with higher average voltage of the ripple diagram and a smaller tertiary turn ratio. With these factors, an optimal turn ratio and inductance can be analyzed for voltage step-up operation of the proposed topology.

When the primary and tertiary turn ratio n is set as 6, this turn ratio is considered with these conditions; maximum voltage applied to the tertiary part is fixed as 360[V] with the formula (32), and 9[V] when the pulsation of the tertiary side V_{Cx} is 1.25%.

$$\left(V_{tri} + V_{Lx} - \frac{\Delta V_{Cx}}{2} \right) \times \frac{N_s}{N_x} > V_{link(\max)} \tag{32}$$

$$V_{Lx} > 101V \tag{33}$$

$$V_{Lx} = L_x \times \frac{\Delta i_3}{\Delta t} \left(where\ \Delta i_3 = \Delta i_1 \times \frac{N_p}{N_x} \approx 3.2A \right) \tag{34}$$

$$L_x = V_{Lx} \times \frac{\Delta T_x}{\Delta i_3} = V_{Lx} \times \frac{d_{dischar} T_s}{\Delta i_3} = 165 \mu H \tag{35}$$

$$L_x \ge 165 \mu H \tag{36}$$

The result of (36) can be achieved by calculating the inductance satisfying the condition of (33), and it is possible to induce tertiary inductance of 165[μH] at least, requiring a larger value at usage.

Also, to prevent distortion of the output current, it is important to maintain a lower ripple value of voltage applied to the decoupling capacity than the voltage of the DC-link, and it

requires a proper design value between the average voltage value of the Ripple port and ripple voltage. So, an optimal capacitance can be induced with the formula below and graph.

$$V_{Cx} = -V_{Cx(avg)} + \sqrt{V_{Cx(avg)}^2 + \frac{V_{AC} I_{AC} T_{AC}}{4\pi C_x}} \quad (37)$$

$$V_{Cx(\min)} = V_{Cx(avg)} - V_x = 2V_{Cx(avg)} - \sqrt{V_{Cx(avg)}^2 + \frac{V_{AC} I_{AC} T_{AC}}{4\pi C_x}} \quad (38)$$

$$V_{Cx(avg)} = \frac{N_x}{N_p} V_{pri} + V_{Lx} = V_{tri} + L_x \frac{\Delta i_3}{T_s \times d_{dischar(\max)}} \quad (39)$$

With the above equations, the average voltage of the Ripple port can be calculated as (39). And using (38) and (39), the waveforms of Fig. 7 can be achieved. The average value of Ripple port voltage is determined by the turn ratio between the primary and tertiary side and the voltage of the tertiary inductor. The final equation (28) shows the relation with the decoupling capacitance and ripple voltage of the tertiary side.

According to Fig. 7, when tertiary inductor L_x value is calculated as 180[μH] using Table II., the dotted line marked part shows the critical value where the maximum value $V_{link(max)}$ of link diagram and the minimum value $V_{Cx(min)}$ of the ripple voltage meet, and the minimum decoupling capacitance is 42[μF]. To prevent distortion of the output current, the decoupling capacitance has to be larger than 42[μF], selecting 50[μF] in consideration of a margin.

In the next design graph, to decide the primary and secondary turn ratios, the design process below is adjusted. The turn ratio can be achieved with a magnetized inductance inducing formula satisfying DCM from (23). With the relational expression of turn ratio and magnetizing inductance, a relation graph can be achieved as shown in Fig. 8.

The dotted line of Fig. 8 is the maximum magnetized inductance satisfying DCM, and when it is supposed the input voltage ranges from a minimum 26.5[V] to a maximum 34[V] in 10[μH] inductance value selected with the design. In this variable input voltage condition, the primary to secondary turn ratio has to be selected within minimum 1.36 and maximum 6.58. In this system, 1:5 is used as an optimal turn ratio.

Fig. 9 shows a relation graph deciding the feasible maximum duty of the main switch based on switching frequency. As the figure below shows, when the switch frequency increases and the same inductance is maintained, the feasible duty increases. In contrast, when the feasible duty is fixed as 0.745 and the switching frequency increases, the magnetized inductance has to be decreased to satisfy DCM.

V. Simulation Results

The proposed topology is designed with a 250[W] flyback inverter for the PV AC-module system and the design specification is shown in Table I. This system is connected with a utility grid of 220[V_{rms}] and 60[Hz]. The simulation was executed by PSIM.

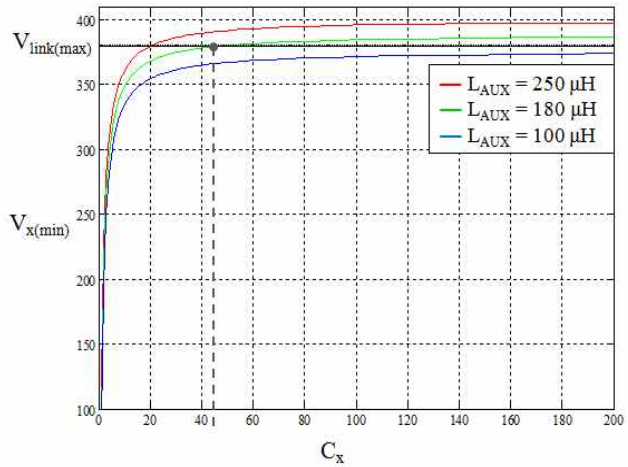

Fig. 7. The relation with Ripple port capacitor C_x and minimum value of ripple voltage $V_{Cx(min)}$.

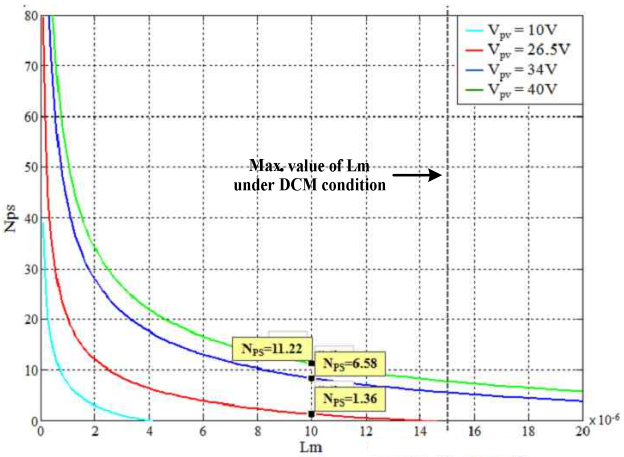

Fig. 8. The relationship between magnetizing inductance and primary to secondary turn ratio with variable input voltage.

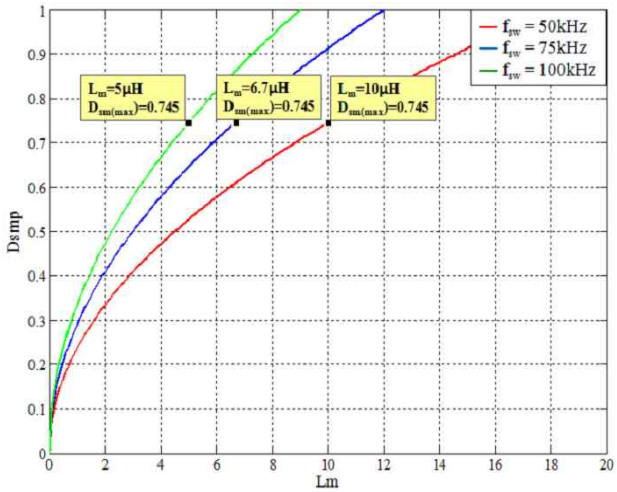

Fig. 9. The relationship between magnetizing inductance and maximum duty of main switch with variable switching frequency.

TABLE I

SPECIFICATION OF PROPOSED CONVERTER

Parameter	Symbol	Value	Unit
Input power	P_{in}	250	W
Input voltage	V_{in}	20 - 40	V
Switching frequency	f_s	50	kHz
Input capacitance	C_{in}	100	μF
Magnetizing inductance	L_m	10	μH
Decoupling capacitance	C_x	50	μF
Ripple port inductance	L_2	180	μH
AC port link capacitance	C_{link}	400	nF
Filter inductance	L_{AC}	6	mH
Filter capacitance	C_{AC}	33	nF
Primary turns	N_p	5	turns
Secondary turns	N_s	25	turns
Tertiary turns	N_x	30	turns
Grid voltage	V_{AC}	220	V_{rms}
Grid frequency	f_{AC}	60	Hz

To verify the above design conditions, simulation in Figs. 10, 11 and 12 show the output current waveform in the case where distortion occurred and did not occur. A passive element of the ripple side is equal, and it is verified by changing the turn ratio between the secondary side and the tertiary side using formula (23). By the turn ratio, tertiary side voltage becomes smaller than the secondary side and the tertiary side energy delivered to the secondary side interval is not formed. Accordingly, the output current shows that distortion occurs.

Fig. 12 shows the current waveforms of each stage, and we can prove the power decoupling process from this result. The proposed active decoupling operation is verified by current through the magnetizing inductor which is shown in the second waveform of Fig. 12. The peak current of the magnetizing inductor $i_{Lm(peak)}$ is 29[A] and this measured value is similar to the theoretical result. Also the Ripple port current i_{Cx} shows the charging and discharging patterns following the principle that the surplus or shortage power decides the charging and discharging processes.

Fig. 13 shows each stage of the waveforms to verify the active power decoupling operation. The first waveform is the output current which has little ringing and distortion. This result occurred from a power unbalancing problem and a leakage inductance series connected in the tertiary port. The second and third waveforms show the input capacitor and decoupling capacitor ripple voltage, respectively. Despite low capacitance on the input side, the ripple voltage across C_{in} has

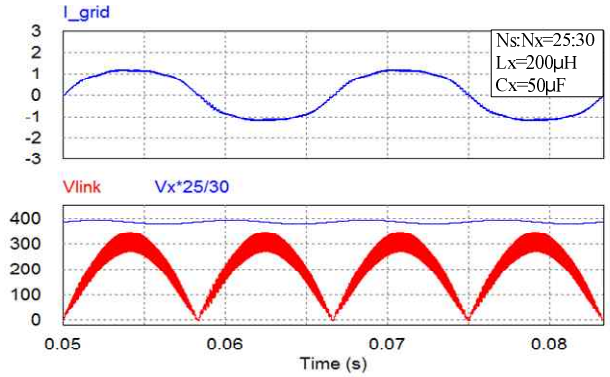

Fig. 10. The waveforms of output current and relation between voltage of decoupling capacitor, V_{Cx} and output voltage of flyback converter, V_{link} (@ N_S:N_X=25:30).

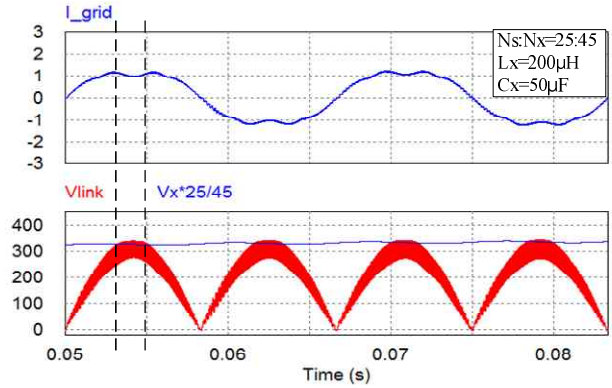

Fig. 11. The waveforms of output current and relation between voltage of decoupling capacitor, V_{Cx} and output voltage of flyback converter, V_{link} (@ N_S:N_X =25:45).

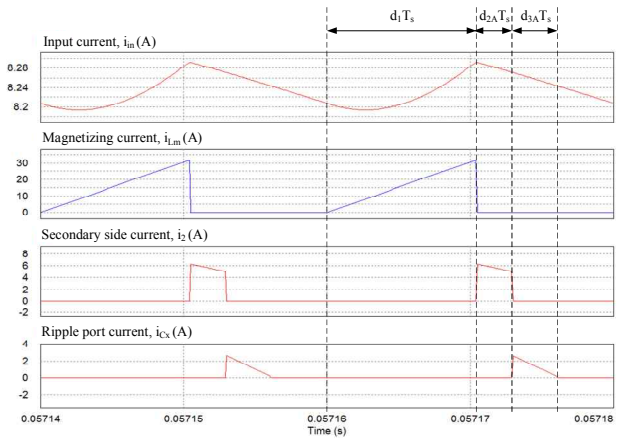

Fig. 12. The waveforms of input, magnetizing, secondary and Ripple port current.

low value under 1[V]. The third wave proves the charging and discharging operation for the decoupling capacitor that has double frequency ripple voltage. So this active power decoupling topology has only switching frequency ripple on the PV side.

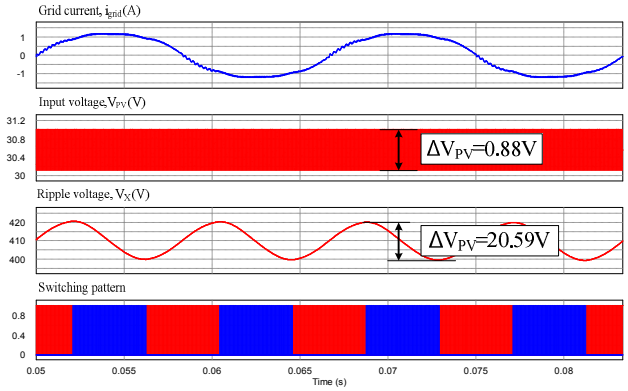

Fig. 13. The waveforms of output current, input voltage, ripple voltage and switching pattern.

VI. Experimental Results

A 250[W] three-port flyback inverter using the active power decoupling method has been experimentally tested. This proposed system is controlled by 32-bit DSP (TMS320F28035, TI) microprocessor. Although the target of this system is LPC250SM, this system uses a PV simulator (E4360, Agilent) as an input source. The validity of the proposed flyback inverter using a three-winding transformer for active power decoupling is experimented by the aforementioned mode analysis, design procedure and calculated duty. The three-winding transformer in this system utilizes the space winding method, to obtain the lowest leakage inductance.

Fig. 14 shows the waveforms of ripple voltage across the input capacitor, ΔV_{in}, output current, I_o and output voltage, V_o. The magnitude of input voltage ripple which is measured only for the AC component is about 600[mV] despite being 800[mV] in simulation results. Fig. 15 shows the waveforms of voltage across the decoupling capacitor, V_{Cx} and voltage across the flyback converter output side, V_{link}. This experimental result represents the possibility of tertiary to secondary energy transfer and proves the design standards as shown in (29) and Fig. 6.

The voltage of the tertiary side is greater than the rectified sine voltage across the output side of the flyback converter, so it can make no distortion of the output current. Fig. 16 shows the waveforms of the AC component of the ripple voltage, $V_{Cx(ac)}$ and output voltage, V_o. This result shows the ripple voltage across the decoupling capacitor with double grid frequency, 120[Hz]. This means that instantaneous power will be transferred to the tertiary side while there is no ripple component with double grid frequency on the PV side. There is a ripple voltage with switching frequency across the input capacitor.

VII. Conclusions

In this paper, a novel active power decoupling flyback inverter for PV-MIC was proposed. To reduce the large input capacitor required for power decoupling in a grid interactive system, we proposed a third Ripple port with auxiliary winding for covering the surplus and shortage energy for diminishing the power differentiation with the DC input and grid. Also a novel switching pattern was adjusted for satisfying the decoupling process. The proposed flyback inverter was verified by simulation and experimental results. Finally, required decoupling capacitance is reduced by Ripple port operation. Thus the life span of the proposed system is able to be longer than conventional AC modules and the system size is also reduced.

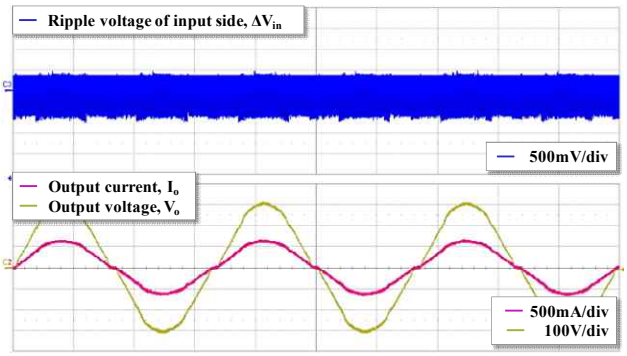

Fig. 14. The waveforms of ripple voltage across input capacitor, ΔV_{in}, output current, I_o and output voltage, V_o.

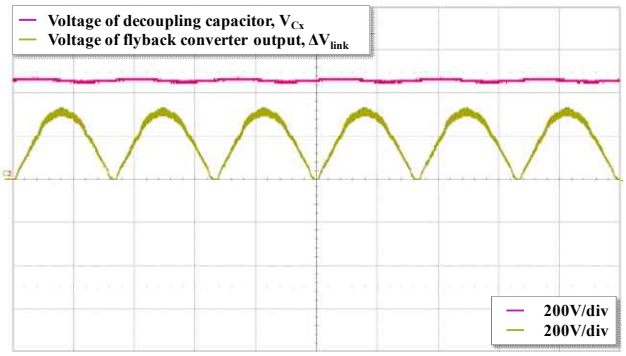

Fig. 15. The waveforms of a voltage across the decoupling capacitor, V_{Cx} and voltage across the flyback converter output side, V_{link}.

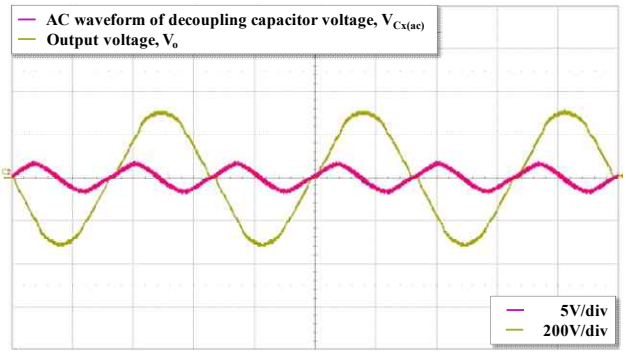

Fig. 16. The waveforms of AC component of ripple voltage, $V_{Cx(ac)}$ and output voltage, V_o.

ACKNOWLEDGMENT

This work was supported by the Human Resources Development of the Korea Institute of Energy Technology Evaluation and Planning (KETEP) grant funded by the Korea government Ministry of Knowledge Economy (No. 20124010203300).

This work was supported by the National Research Foundation of Korea(NRF) grant funded by the Korea government(MEST) (No.2011-0015584)

REFERENCES

[1] S. B. Kjaer, J. K. Pedersen, and F. Blaabjerg, "A review of single-phase grid-connected inverters for photovoltaic modules," *IEEE Trans. Ind. Appl.*, Vol. 41, No. 5, pp. 1292-1306, Sep. 2005.

[2] Y. Xue, L. Chang, S. B. Kjaer, J. Bordonau, and T. Shimizu, "Topologies of single-phase inverters for small distributed power generators: an overview," *IEEE Trans. Power Electron.,* Vol. 19, No. 5, pp. 1305-1314, Sep. 2004.

[3] Q. Li and P. Wolfs, "A review of the single phase photovoltaic module integrated converter topologies with three different DC link configurations," *IEEE Trans. Power Electon*., Vol. 23, No. 3, pp. 1320-1333, May 2008.

[4] S. B. Kjaer, "Design and control of an inverter for photovoltaic applications," Ph.D. dissertation, inst. Energy Technol., Aalborg University, Aalborg East, Denmark, 2004/2005.

[5] H. Hu, S. Harb, N. KutKut, I. Batarseh, and Z. J. Shen, "Power decoupling techniques for micro-inverters in PV systems-a review," *IEEE Energy Conversion Congress and Exposition*, pp. 3235-3240, Sep. 2010.

[6] P. T. Krein and R. S. Balog, "Method for minimizing double-frequency ripple power in single-phase power conditioners," U.S. Patent Application No. 11/871,015, filed Oct 11, 2007.

[7] G. H. Tan, J. Z. Wang, and Y. C. Ji, "Soft-switching flyback inverter with enhanced power decoupling for photovoltaic applications," *IET Trans. Electron. Power Appl*., Vol. 1, No. 2, pp. 264-274, Mar. 2007.

[8] A. C. Kyritsis, N. P. Papanikolaou, and E. C. Tatakis, "A novel parallel active filter for current pulsation smoothing on single stage grid-connected AC-PV modules," *in Proc. European Conf. Power Electronics and Applications (EPE),* pp. 1-10, Sep. 2007.

[9] T. Shimizu, K. Wada, and N. Nakamura, "Flyback-type single-phase utility interactive inverter with power pulsation decoupling on the DC input for an AC photovoltaic module system," *IEEE Trans. Power Electron.*, Vol. 21, No. 5, pp.1264-1272, Sep. 2006.

[10] T. Shimizu, K. Wada, and N. Nakamura, "A flyback-type single phase utility interactive inverter with low-frequency ripple current reduction on the DC input for an AC photovoltaic module system," *in Proc. IEEE 33rd Annu. Power Electron. Spec. Conf. (PESC),* Vol. 3, pp. 1483-1488, 2002.

[11] T. Hirao, T. Shimizu, M. Ishikawa, and K. Yasui, "A modified modulration control of a single-phase inverter with enhanced power decoupling for a photovoltaic AC module," *in Proc. Eur. Conf. Power Electron. Appl*., 2005.

[12] F. Shinjo, K. Wada, and T. Shimizu, "A single-phase grid-connected inverter with a power decoupling function," *in Proc. Power Electron. Spec. Conf. (PESC)*, pp. 1245-1249, Jun. 2007.

[13] T. Shimizu and S. Suzuki, "Control of a high-efficiency PV inverter with power decoupling function," *in Proc. IEEE 8th Inter. Conf. Power Elec. and ECCE Asia (ICPE & ECCE),* No. 1533-1539, 2011.

[14] S. B. Kajer and F. Blaabjerg, "Design optimization of single phase inverter for photovoltaic applications," *in Proc. IEEE PESC '03 Conf.*, Vol. 3, pp. 1183-1190, Jun. 2003.

[15] D. Li, Z. Zhang, B. Xu, M. Chen, and Z. Qian, "A method of power decoupling for long life micro-inverter," *in Proc. 37th Annu. Conf. on IEEE Indus. Elec. Soc. (IECON 2011)*, pp. 802-807, Nov. 2011.

[16] P. T. Krein and R. S. Balog, "Cost-effective hundred-year life for single-phase inverters and rectifiers in solar and LED lighting application based on minimum capacitance requirements and a ripple power port," *in Proc. IEEE Applied Power Elec. Conf*., pp. 620-625, Feb. 2009.

[17] H. Al-Atrash, F. Tian, and I. Batarseh, "Tri-modal half-bridge converter topology for three-port interface," *IEEE Trans. Power Electron.*, Vol. 22, No. 1, pp. 341-345, Jan. 2007.

[18] H. Hu, Q. Zhang, X. Fang, Z. J. Shen, and I. Batarseh, "A single stage micro-inverter based on a three-port flyback with power decoupling capability," *in Proc. Energy Conversion Congress and Exposition (ECCE),* pp. 1411-1416, Sep. 2011.

[19] S. Harb, N. KutKut, I. Batarseh, and Z. J. Shen, "A three-port photovoltaic (PV) micro-inverter with power decoupling capability," *Applied Power Electronics Conference and Exposition (APEC),* pp. 203-208, 2011.

[20] Y. M. Chen and C. Y. Liao, "Three-port flyback-type single-phase micro-inverter with active power decoupling circuit," *in Proc. Energy Conversion Congress and Exposition (ECCE),* pp. 501-506, Sep. 2011.

[21] A. C. Kyritsis, E. C. Tatakis, N. P. Papanikolaou, "Optimum design of the current-source flyback inverter for decentralized grid-connected photovoltaic systems," *IEEE Trans. Energy Convers.,* Vol. 23, No. 1, pp. 281-293, Mar. 2008.

Jun-Gu Kim was born in Korea, in 1981. He received the M.S. degree from the Graduate College of Photovoltaic System Engineering, Sungkyunkwan University, Suwon, Korea, in 2009, where he is currently working toward the Ph.D. degree. His research interests include converters, inverters, bidirectional converter, battery charging/discharging and its control for renewable energy applications.

Kyu-Dong Kim was born in 1986 in Korea. He received the B.S. degree in Faculty of Electronic Engineering from Sungkyunkwan univertisy, and M.S. degree in College of Information and Communication Engineering from Sungkyunkwan University, Suwon, Korea, in 2011 and 2013, respectively. He is currently an assistant engineer in the SAMSUNG Electro-Mechanics.

Yong-Su Noh was born in 1985 in Suwon, Korea. He received the B.S. degree in Electrical and Computer Engineering from Ajou University, Suwon, Korea. He is currently working toward the Combined Master/Ph.D degree in College of Information and Communication Engineering from Sungkyunkwan University, Suwon, Korea. His research interests include converters, inverters, and its control for renewable energy application.

Yong-Chae Jung was born in Korea in 1965. He received the B.S. degree from Hanyang University, Seoul, Korea, in 1989, and the M.S. and Ph.D. degrees in Electrical Engineering from the Korea Advanced Institute of Science and Technology (KAIST), Daejeon, Korea, in 1991 and 1995, respectively. He is currently a professor in the department of Electronic Engineering at Namseoul University. His research interests include design and control of power converters, soft switching power converters, resonant power circuits, photovoltaic system, power factor corrections, SMPS, induction heating circuit and EMI suppression. He is a member of the Korea Institute of Power Electronics (KIPE), and Korea Institute of Electrical Engineering (KIEE).

Chung-Yuen Won was born in Korea in 1955. He received the B.S. degrees in Electrical Engineering from Sungkyunkwan University, Suwon, Korea, in 1978, and the M.S. and Ph.D. degrees in Electrical Engineering from Seoul National University, Seoul, Korea, in 1980 and 1987, respectively. From 1990 to 1991, he was with the Department of Electrical Engineering, University of Tennessee, Knoxville, as a Visiting Professor. Since 1988, he has been with a member of the faculty of Sungkyunkwan University, where he is a Professor in the College of Information and Communication Engineering; also he is the director of Samsung Energy Power Research Center. He was the President of the Korean Institute of Power Electronics in 2010. Since 2011, he has been a director of the Korean Federation of Science and Technology Societies. His current research interests include the power electronic of electric machines, electric/hybrid vehicle drives, power converters for renewable energy systems. He is a senior member of the Institute of Electrical and Electronics Engineers (IEEE).